*Small Methods*

small methods
www.small-methods.com

RESEARCH ARTICLE OPEN ACCESS

# Motorized DNAzymes Drive Enhanced Electrochemical Biosensing for Rapid Bacterial Detection

Amir Ali Akhlaghi[1] | Sadman Sakib[2] | Roderick MacLachlan[2] | Jinal Manek[2] | Enas Osman[1] | Survanshu Saxena[1] | Ehsan Heydarian Dolatabadi[1] | Jimmy Gu[3] | Yingfu Li[1,3,4] | Leyla Soleymani[1,2,3,4]

[1]School of Biomedical Engineering, McMaster University, Hamilton, Ontario, Canada | [2]Department of Engineering Physics, McMaster University, Hamilton, Ontario, Canada | [3]Department of Biochemistry and Biomedical Sciences, McMaster University, Hamilton, Ontario, Canada | [4]Institute for Infectious Disease Research, McMaster University, Hamilton, Ontario, Canada

**Correspondence:** Yingfu Li (liying@mcmaster.ca) | Leyla Soleymani (soleyml@mcmaster.ca)

**Received:** 16 October 2025 | **Revised:** 15 February 2026 | **Accepted:** 23 February 2026

**Keywords:** biosensors, DNAzymes | electrochemistry | legionella pneumophila | micromotors

## ABSTRACT

Self-propelled micromotors hold great promise for improving the performance of electrochemical biosensors by overcoming mass transport limitations inherent to target recognition on electrode surfaces. However, the successful integration of micromotors in electrochemical biosensors for the analysis of crude biological samples has remained elusive. In this study, we introduce the Motolyzer, a micromotor-based assay that utilizes DNAzymes for the identification and detection of bacterial targets in crude biological samples. In this system, immobilized DNAzymes are propelled by magnetic-layered micromotors within biological samples. Upon encountering their specific targets, these DNAzymes release redox DNA barcodes, which are subsequently analyzed using electrochemical chips. The Motolyzer significantly enhances the target-to-blank ratio of the biosensor (4.5 times) and achieves a limit-of-detection of $2 \times 10^4$ CFU $mL^{-1}$ for *Legionella pneumophila*, a slow-growing bacterium, within 1 h, thereby eliminating the need for bacterial culture. Notably, the Motolyzer exhibits high specificity against non-target bacterial strains as well as non-bacterial metabolites, establishing it as a reliable, rapid assay for the identification of specific bacteria in crude biological samples. The versatility of this approach opens promising avenues for the rapid detection of various pathogens and biomarkers in both clinical and environmental settings.

## 1 | Introduction

Biosensors are tasked with identifying specific target molecules in a large amount of biological background material available within a sample matrix [1]. The operation of surface-based biosensors, such as electrochemical biosensing, relies on the transport of target analytes from the sample to the biosensor surface, specific interactions between the target and the biorecognition elements, and target-induced signal transduction [2]. Building biosensors with improved analytical performance increased sensitivity and specificity at a faster response time is a multi-pronged approach focused on increasing mass transport rates, binding affinity, and signal transduction efficiency, while reducing nonspecific binding [3].

Enhancing mass transport is particularly important in biosensors since even the most sensitive biorecognition elements and signal transducers fail to make a difference if a sufficient number of target analytes are not accumulated on the transducer surface [4]. To overcome the mass transport challenges of biosensors, active transport methods such as fluidic flow [5] and mixing [6] have been used to bring targets to biorecognition elements at a faster rate or increase the probability of collisions. In the context of fluidic flow, pump-based [7–9], pump-free [10, 11], and manual

pumping [12] systems have been employed in biosensors for the detection of target analytes. Although these strategies vary in complexity, incorporating them into biosensing devices requires extra equipment, manufacturing processes, or operational procedures, which increases both the overall cost and complexity of the system [12, 13]. In the context of mixing that does not rely on fluidic flow, manual pipetting is the simplest method; however, it is associated with user-dependent variability [14, 15]. External fields such as magnetic fields for displacing magnetic colloidal particles [16, 17], electric fields for iontophoretic mixing [18, 19], and acoustic fields for generating ultrasonic vibrations or surface acoustic waves [20, 21] have also been implemented for use in biosensors. Even though these devices overcome the user-dependent variability of manual mixing, they rely on external transducers, which, like flow-based systems, add to the system complexity.

Our goal was to develop mixing methods that, like existing field-based approaches, enhance biosensor performance by reducing diffusion-limited detection times [22], yet do not require external actuators. Furthermore, we were interested in strategies that could be integrated into electrochemical biosensing systems. Inspired by biomolecular motors that enable active transport of analytes between cells [23], there is great interest in using colloidal micromotors to increase mass transport rates in biosensors. In the context of electrochemical biosensing, tubular [24–28], Janus [29–31], and non-Janus/spherical [32–34] micromotors have been used to enhance the interaction between biorecognition elements and target analytes [24, 26–29, 32–35].

Tubular micromotors have recently been applied in electrochemical biosensing assays (Table S1). In one example, magnetic reduced graphene oxide/Ni/PtNP micromotors were functionalized with antibodies against C-reactive protein and used to detect neonatal sepsis markers in under 10 min [25]. Target capture occurred through antibody–antigen binding on the motor surface, while signal generation relied on horse radish peroxidase-mediated electrochemical reaction. The autonomous propulsion of the micromotors enhanced antibody–antigen collision frequency, improving sensitivity and reproducibility compared to static assays [25]. Building on this, a microfluidic thin-layer gold chip was integrated with graphene/Ni/PtNP micromotors, also loaded with anti-C-reactive protein antibodies [24]. In this platform, C-reactive protein antigens were captured on the moving motors, transported into the confined microfluidic chamber, and electrochemically quantified. The active motion both accelerated transport into the sensing zone and minimized nonspecific adsorption, enabling rapid and reproducible amperometric detection of C-reactive protein in neonatal plasma [24]. For Alzheimer's diagnostics, polypyrrole/Ni/PtNP micromotors were coated with anti-A$\beta$42 antibodies to create a sandwich-type immunoassay for analyzing brain tissue, cerebrospinal fluid, and plasma [36]. The captured A$\beta$42 was recognized by an HRP-labeled secondary antibody, with the resulting hydroquinone/$H_2O_2$ redox cycling measured amperometrically on a magnetically fixed electrode. Self-propulsion accelerated biorecognition, allowing reliable quantification from just 25 µL of sample within 15 min and achieving a limit-of-detection of 0.06 ng mL$^{-1}$ [36]. A complementary approach employed graphene oxide/AuNP/Ni/PtNP micromotors modified with a thiolated aptamer specific to A$\beta$42 oligomers [27]. Recognition occurred on-the-fly during motor motion, and binding events impeded the redox probe $[Fe(CN)_6]^{3-/4-}$ at the electrode surface, producing a square-wave voltammetry signal. The catalytic AuNPs enhanced propulsion speed two-fold and aptamer immobilization efficiency, enabling ultrasensitive and label-free detection of A$\beta$42 oligomers down to 0.10 pg mL$^{-1}$ in as little as 5 µL of plasma, cerebrospinal fluid, or brain tissue [27]. Collectively, these examples highlight how integrating carbon-based tubular micromotors with electrochemical transducers enhances assay kinetics, reduces diffusion limitations, and improves sensitivity in clinically-relevant complex samples compared to static conditions.

Although fluorescence-based microplate readers are common in laboratory workflows, electrochemical detection provides complementary benefits for point-of-care use, including low-cost instrumentation, miniaturization, and suitability for portable diagnostic devices, as evident by the success of the glucose monitor. These characteristics make electrochemical detection particularly well-suited for integrating micromotor-enhanced assays into low-cost diagnostic platforms.

Despite these advances, no prior work has used DNAzymes to construct micromotor-based biosensing systems. As a result, there has been no demonstration of integrating RNA-cleaving DNAzymes with micromotors for catalytic biosensing, nor a strategy that couples micromotor propulsion with DNAzyme-mediated barcode release for electrochemical detection. This represents an important gap given that RNA-cleaving DNAzymes can be selected in vitro for virtually any target of interest and therefore offer a uniquely adaptable catalytic modality rather than simple affinity-based binding [37].

Our vision was to create an assay that enhances target capture through the active movement of biorecognition elements across a sample using micromotors, while ensuring that the micromotors do not interfere with signal transduction on an electrode surface. This is challenging to achieve using biorecognition elements such as antibodies or aptamers, where a sandwich format is needed to combine biorecognition with signal transduction. In contrast, RNA-cleaving DNAzymes are a class of functional nucleic acids that can be selected in vitro to identify a specific target molecule and release a DNA barcode in response, eliminating the need for a sandwich configuration for signal transduction. The structure switching ability of these DNAzymes makes them ideally suited for developing micromotor-based biosensors that could actively search samples for target analytes and generate a signalling element that can be detected using standard transductors without micromotor interference. Because this released DNA barcode is directly compatible with electrochemical readout, DNAzymes provide a natural bridge between autonomous target search (enabled by micromotors) and sensitive signal transduction on an electrode surface. Yet in conventional static formats, the efficiency with which DNAzymes encounter their targets can be limited, particularly in heterogeneous or diffusion-restricted samples. Combining them with autonomous micromotor propulsion offers a previously unexplored strategy to overcome these limitations. The ability of micromotors to actively transport DNAzymes through complex samples provides a unique solution to the long-standing mass-transport challenges of catalytic nucleic acid sensors.

The practical value of this integration is supported by prior work showing that RNA-cleaving DNAzymes can enable culture-free pathogen detection in clinically relevant samples. For example, in a previous study from our group, RCD-based urinary tract infection diagnostics exhibited strong analytical performance but were limited by mixing-dependent linearity in static formats [38]. Incorporating autonomous micromotor propulsion offers a direct strategy to overcome such mass-transport constraints, broadening the usability of catalytic nucleic acid assays in real diagnostic scenarios.

Herein, we demonstrate the micromotor DNAzyme Analyzer (Motolyzer), which leverages advanced materials such as RNA-cleaving DNAzymes and micromotors for simplifying the operation of biosensors. The Motolyzer employs bacteria-specific DNAzymes that are assembled on micromotors to enhance bacterial identification in crude biological samples. To our knowledge, this is the first platform to integrate RNA-cleaving DNAzymes with micromotors for electrochemical barcode-based sensing, establishing a new approach for motor-powered catalytic biosensing. As a proof-of-concept, we apply the Motolyzer for the detection of *Legionella pneumophila*, a slow-growing waterborne pathogen and the causative agent of Legionnaires' disease, which presents significant public health concerns due to its persistence in water systems [39]. The Motolyzer demonstrates the advantages of active mixing, which significantly enhances both the limit-of-detection and the signal-to-blank ratio of the assay compared to passive conditions or setups that use manual agitation. By eliminating cumbersome procedures such as mixing and reagent addition, the Motolyzer offers a viable platform for point-of-care testing.

## 2 | Results and Discussion

### 2.1 | Creating the Motolyzer

The Motolyzer integrates three key components: (1) magnetic-layered micromotors (M2 Motors) that deliver biorecognition elements to target analytes through propulsion in the biosensing medium, while ensuring compatibility with magnetic separation (Figure 1ai); (2) RNA-cleaving DNAzymes functionalized on the micromotors, programmed to navigate the biosensing medium and release a DNA barcode upon encountering proteins released from bacterial cells (Figure 1aii); [40] and (3) electrochemical chips (e-chips) equipped with 3D hierarchical gold electrodes designed to capture DNA barcodes with enhanced hybridization efficiency compared to their planar counterparts for generating an electrochemical signal (Figure 1aiii) [13, 38]. The Motolyzer is engineered to enable advanced materials to perform autonomously, reducing the need for user intervention and enhancing assay speed [41].

The assay operation is simple: a drop of sample solution is added to a vial pre-filled with DNAzyme-modified M2 Motors, followed by an incubation period (Figure 1b,c). In instances where a positive sample is present, specific bacterial proteins interact with the DNAzymes throughout the incubation period. This interaction results in the release of DNA barcodes that are modified with the redox moiety methylene blue (release phase). Following the incubation period, the vial is placed in a magnetic holder that effectively separates M2 Motors, thereby preventing any interference with the electrochemical signal readout (separation phase). Subsequently, the e-chips are inserted into the vial for a second incubation period (capture phase). During this capture phase, the DNA barcodes are captured by their complementary DNA probes. The proximity of methylene blue to the surface of the gold electrodes following hybridization results in an electrochemical reduction peak, which is measured using square wave voltammetry (readout phase). It is expected that an increase in bacterial concentration will lead to a higher concentration of the target protein, which will subsequently result in a greater number of cleaved DNA barcodes [38]. As a result, the intensity of the electrochemical current is anticipated to rise with an increase in bacterial concentration.

### 2.2 | Characterizing the M2 Motors

We aimed to create trifunctional M2 Motors that can be easily functionalized with DNAzymes, actively propelled by a chemical fuel, and magnetically separated (Figure 2ai-iii). Specifically, the M2 Motors combine an outer layer of reduced graphene oxide (rGO) that serves as a carboxyl-rich backbone for the conjugation of aminated DNAzymes with inner layers of metallic nickel (Ni) and platinum nanoparticles (PtNP) for magnetic separation and active propulsion, respectively. The M2 Motors are constructed through a layer-by-layer electrodeposition of rGO, nickel (Ni), and platinum nanoparticles (PtNP) through a template created from a polycarbonate membrane that has been sputtered with gold (Figure 2b). During the electrodeposition of each layer, the current signal was continuously monitored to ensure successful material deposition (Figure S1a–c).

A comprehensive structural characterization was performed to confirm the successful fabrication of tubular rGO/Ni/PtNP/DNAzyme M2 Motors. Scanning Electron Microscopy (SEM) images demonstrated that the resulting M2 Motors are hollow tubes decorated with nanoparticles with an inner radius of 2.1 μm and a length of 10–15 μm. (Figure 2ci,ii). The presence of key elements in M2 Motors (Pt and Ni) was further confirmed with Energy Dispersive Spectroscopy (EDS) (Figure 2d), confirming the successful electrodeposition of the inner layers. Fourier-Transform Infrared (FT-IR) spectroscopy demonstrates a peak at 2367 $cm^{-1}$, indicating the presence of aldehyde functional groups (Figure 2e) [42]. A peak at 1760 $cm^{-1}$, corresponding to carbonyl stretches caused by carboxylic acid groups present in rGO [43], and peaks observed at 1045 and 1249 $cm^{-1}$ related to the presence of epoxide and other oxygen-containing functional groups can be observed. For M2 Motors modified with aminated DNAzymes, an additional stretch at 1556 $cm^{-1}$ suggests the presence of DNA nitrogenous bases [44], while the peak at 3543 $cm^{-1}$ may indicate methylene blue adsorbed onto the outer layer of rGO [45]. Conjugation of DNAzymes on M2 Motors was further evaluated with X-ray Photoelectron Spectroscopy (XPS) (Figure 2f) [46]. The spectra indicate that the O1s signal is more pronounced than the C1s signal, consistent with previous reports on rGO-based micromotors [46]. The high-resolution peaks of the C1s and O1s spectra correspond to the binding energies of various functional groups, including C═C, C—C / C—H, C═O, O—C═O, and O—H. This analysis reveals the nature of the covalent bonds between carbon and

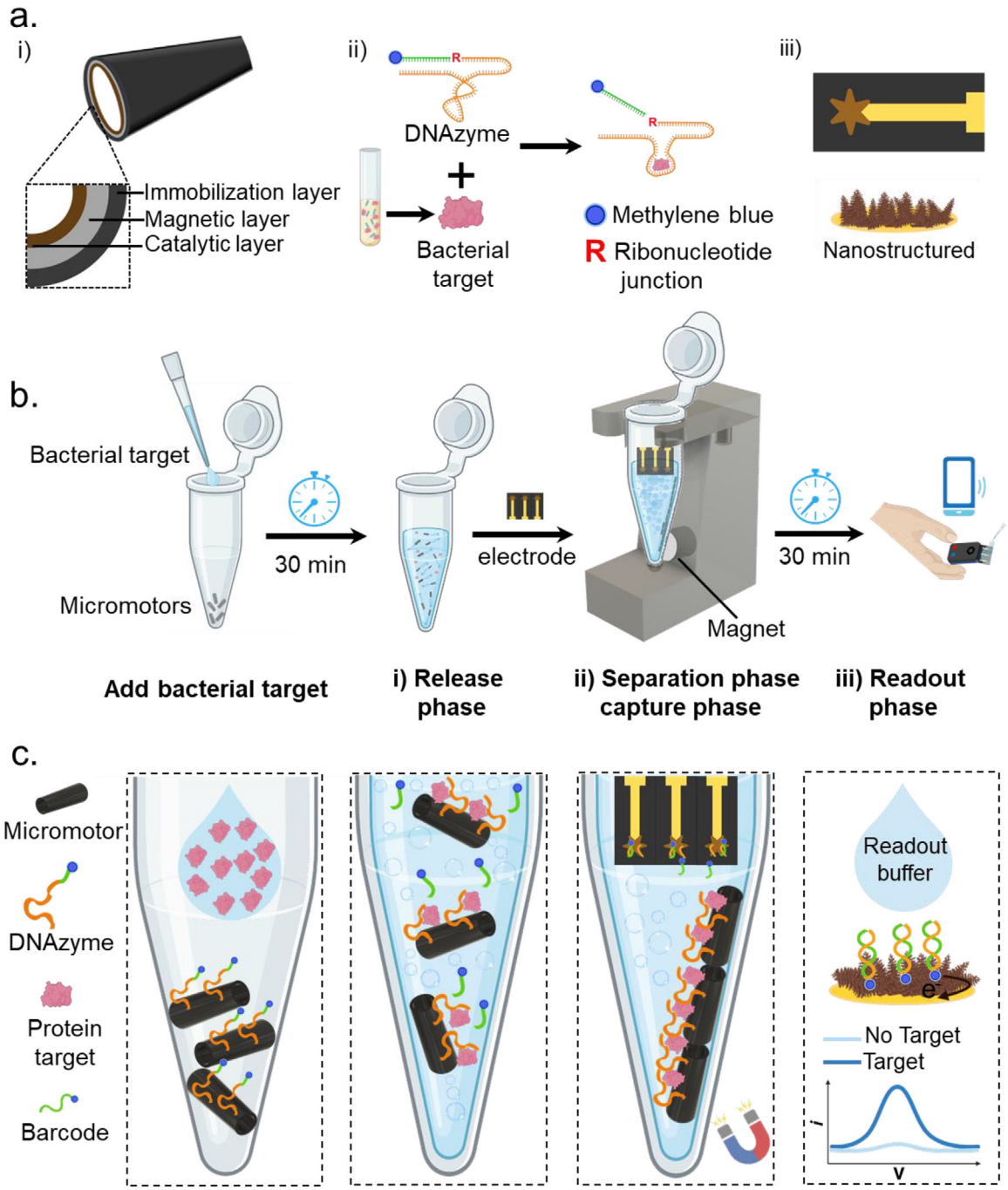


**FIGURE 1** | Schematic illustration of the Motolyzer. (a) Building blocks of the Motolyzer: (i) M2 Motors, (ii) RNA-cleaving DNAzymes modified with the redox label methylene blue, and the (iii) star-patterned hierarchical gold electrode with nanostructures. (b) Overview of the assay operation at the macro- (b) and micro- (c) scales, divided into: (i) the release phase, (ii) the separation and capture phase, and (iii) the readout phase. The target solution comprises the crude extracellular matrix derived from bacteria, along with fuel and surfactant.

oxygen atoms (Figure 2gi,ii). The high-resolution N1s spectra of DNAzymes at 397.8 and 399.4 eV correspond to imine (-N =) and amine (-$NH_2$) groups (Figure 2giii). The slight negative shift in binding energy for the imine group at 397.8 eV, compared to the reported range of 399–400 eV, may be attributed to the adsorption of DNAzyme onto the M2 Motors, as documented in previous studies [47]. Lastly, the high-resolution S2p' spectra showed a positive shift in binding energy (167.1 and 168.1 eV), which could be attributed to the oxidized sulfur found in methylene blue during sample preparation and handling, which aligns with previously reported binding energy ranges (167–169 eV) for oxidized sulfur-containing species (Figure 2giv) [48]. These findings demonstrate the successful fabrication of M2 Motors with an outer rGO layer that successfully houses DNAzymes for creating the Motolyzer.

Following structural characterization, we evaluated the functionality of M2 Motors. To assess active propulsion, we imaged the fabricated micromotors under varying concentrations of $H_2O_2$ and sodium cholate as the fuel and surfactant,

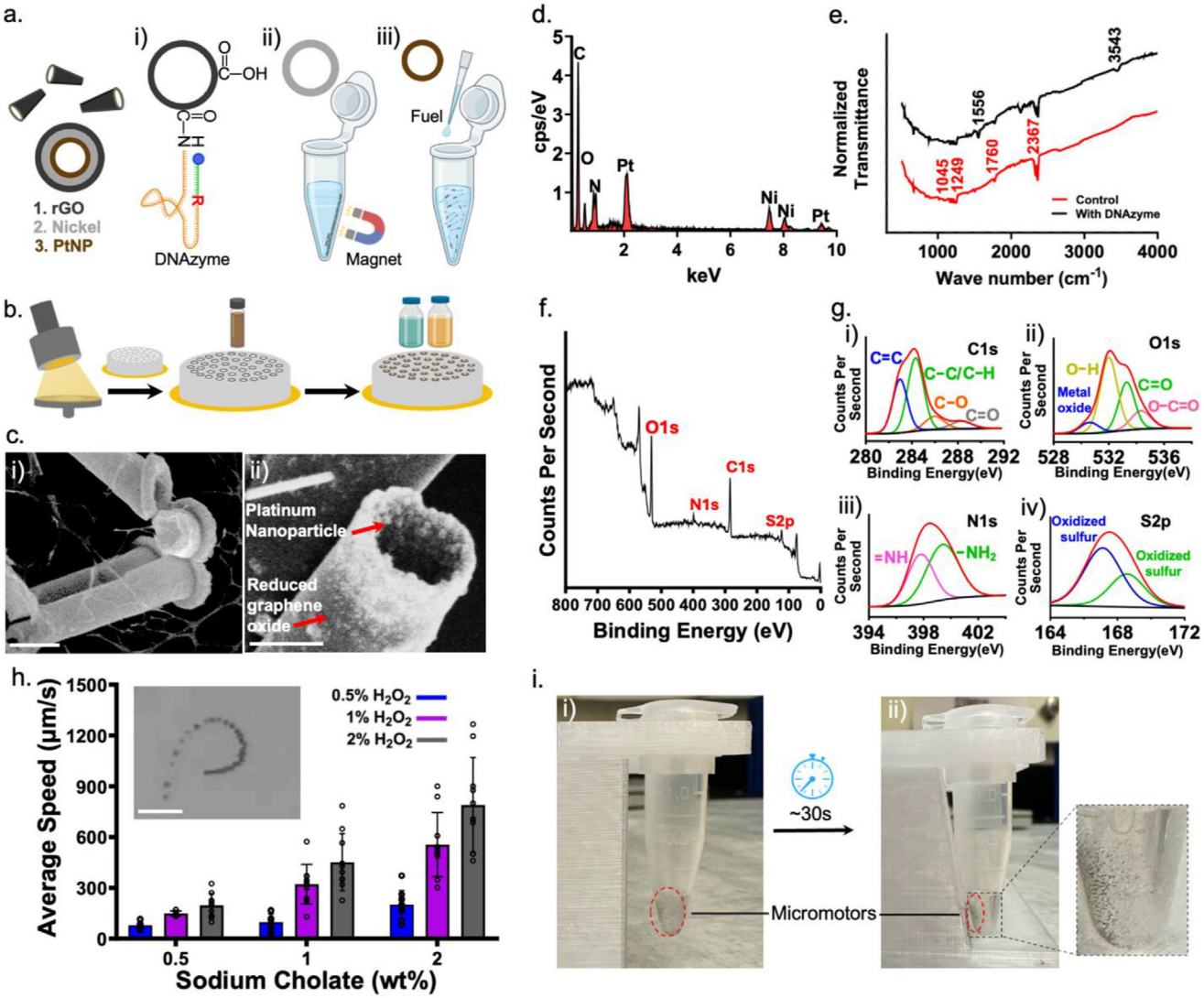


**FIGURE 2** | Fabrication and characterization of M2 Motors. (a) Schematic illustration showcasing the capabilities of M2 Motors, including: (i) molecular modification, (ii) magnetic separation, and (iii) active propulsion. (b) Schematic illustration demonstrating the stepwise fabrication of M2 Motors, involving sputtering on a polycarbonate membrane with gold, electrodepositing the outer rGO layer, and electrodepositing the inner metallic layers. (c) SEM images of micromotors. Scale bar: (i) 4 μm (ii) 6 μm. (d) Characterization of micromotors using electron diffraction spectroscopy (EDS). (e) Fourier-Transform Infrared (FT-IR) spectroscopy showing before and after immobilization of DNAzymes. (f) X-ray photoelectron spectroscopy (XPS) survey of DNAzyme-functionalized M2 Motors, showing C1s, O1s, N1s, and S2p spectra. (g) High-resolution XPS spectra of DNAzyme-functionalized M2 Motors showing various functional groups for (i) carbon (C1s), (ii) oxygen (O1s), (iii) nitrogen (N1s), and (iv) sulfur (S2p). (h) Summary of mean speed from 10 micromotors under varying fuel ($H_2O_2$) and surfactant (sodium cholate) concentrations. The inset shows a propelled M2 Motor. Scale bar: 25 μm. (i) Digital images of M2 Motors in the absence (i) and presence (ii) of a magnet.

respectively (Figure S2a). The presence of $H_2O_2$ results in generation of oxygen bubble tails from either opening of micromotors, while the presence of sodium cholate serves to lower the surface tension to allow for efficient propulsion in the biosensing medium [49]. An increase in mean instantaneous speed is observed with increasing concentration of fuel or surfactant (Figure 2h), which is consistent with previous reports (Table S2) [50]. This increase in instantaneous speed is further supported using trajectory maps, where higher $H_2O_2$ levels result in longer, more directed paths (Figure S2b). Such speeds (103 μm/s at 0.2% $H_2O_2$, 152 μm/s at 0.5% $H_2O_2$, 400 μm/s at 1% $H_2O_2$, and 800 μm/s at 2% $H_2O_2$) are comparable to those previously reported in the literature, demonstrating a range of 150–600 μm/s depending on the type and concentration of the solution used (Figure 2h; Table S2). These data confirm that the micromotors maintain active propulsion at 0.5% $H_2O_2$, the concentration used in all bacterial sensing assays.

Lastly, we evaluated whether the assay medium impacts the swimming capability of the micromotors by performing mean square displacement analysis (Figure S2c; Videos S1–S5). A higher mean square displacement slope was observed in buffer compared to crude bacterial culture used in this assay at both 0.5% and 1% $H_2O_2$. For instance, at 1% $H_2O_2$, micromotors in buffer reached mean square displacement values near $2.0 \times 10^5$ $\mu m^2$ after 3 s; whereas, those in crude culture plateaued around $1.3 \times 10^5$ $\mu m^2$. This slight reduction in motility in the crude medium is likely due to matrix effects, as previous studies have

reported that increased viscosity, presence of macromolecules, or nonspecific interactions in complex biological fluids can hinder bubble growth and propulsion efficiency, thereby limiting long-range micromotor transport while still preserving active motion at shorter distances [51]. Importantly, all analytical performance measurements reported in this study—including limit of detection, sensitivity, and signal-to-blank enhancements—were obtained under the same 0.5% $H_2O_2$ propulsion conditions used in sensing assays, ensuring that performance improvements arise from biologically compatible operation.

We further evaluated the magnetic separation capabilities of the M2 Motors by subjecting them to a relatively weak magnetic field generated by a neodymium magnet (Figure 2i). This process led to a magnetic separation in just 30 s, confirming the magnetic capabilities of the M2 Motors.

### 2.3 | Assessing the Analytical Performance of the Motolyzer

We utilized the Motolyzer platform to create a rapid method for analyzing water samples for *L. pneumophila* (Legionella Motolyzer). This slow-growing and lethal bacterium is the causative agent of Legionnaires' disease, a serious respiratory infection that presents considerable public health risks [39]. The World Health Organization reports that the presence of this bacterium in drinking water systems has risen due to aging infrastructure and climate change, thus requiring rapid and accessible detection methods [52]. Current detection methods, including culture-based assays and polymerase chain reaction, are labor-intensive, require skilled personnel, and can take several days to produce results, presenting a gap in rapid testing technologies for detecting *L. pneumophila* [53].

In response, the Legionella Motolyzer was created by immobilizing *L. pneumophila* DNAzymes on M2 Motors and depositing DNA capture probes on e-chips. To assess the biocatalytic activity of the DNAzyme and the structural compatibility of the crude bacterial protein target in the presence of $H_2O_2$ and sodium cholate, DNAzymes were incubated with stock crude bacterial targets containing varying concentrations of either $H_2O_2$ or sodium cholate, and the resulting products were analyzed by denaturing polyacrylamide gel electrophoresis (Figure S3). A decrease in cleavage efficiency with increasing concentration of $H_2O_2$ and sodium cholate is observed due to oxidizing effects on the DNAzyme or protein target, as reported previously [54]. As such, we chose the $H_2O_2$ and sodium cholate concentration of 0.5%, at which point active propulsion was coupled to a reasonable cleavage efficiency.

The gold surface was activated with successive cleaning using cyclic voltammetry (Figure S4a) prior to capture probe immobilization. Cyclic voltammetry was further used to confirm the immobilization of the capture probe using gold-thiol chemistry as well as the backfilling of exposed gold (Figure S4b). During the assay operation, the gold electrodes were briefly exposed ($\leq$30 min) to $\leq$0.5% $H_2O_2$. Under these conditions, and following a simple rinse before the readout phase, no visible corrosion or deterioration in electrode morphology or electrochemical response was observed.

To maximize the signal-to-blank ratio measured using the Motolyzer, we optimized the density of capture probes and blocking layers on the e-chips (Figure S5), as well as the amount of blocking layers on the M2 Motors (Figure S6). The density of the capture probe and the blocking layer was optimized by increasing the concentration of the capture probe across three different incubation times while maintaining the backfiller concentration constant. We used 6-mercapto-1-hexanol (MCH) as the backfiller, which has been widely applied in electrochemical DNA biosensors for reducing nonspecific binding [55]. In this optimization study, an increase in signal magnitude was observed with increasing capture probe concentration (0.5-2 μM) under all backfilling time-points (10–60 min), except for a decrease in signal for the highest capture probe concentration (4 μM) (Figure S5). This finding is explained by previous reports, where signal magnitude drops by ≈10% at high probe densities due to overpacking of the self-assembled monolayer, decreasing the hybridization efficiency between two DNA strands [55]. As such, we chose 2 μM as the concentration of capture probe for the rest of this study. In parallel, we optimized the amount of blocking layers (tween) used on the M2 Motors to achieve the highest signal-to-blank ratio (Figure S6). More specifically, we evaluated the effect of surface blocking on DNAzyme-modified M2 Motors by using Tween20 as a surface blocker across two different target concentrations. Interestingly, we noticed a 4-fold increase in signal magnitude for the detection of crude bacterial target with overnight surface blocking using Tween20 as compared to no surface blocking (Figure S6). We speculate that the effective blocking of Tween20 on rGO [56] and its derivatives serves a crucial role in preventing non-specific adsorption of the nitrogenous bases of the DNAzyme, resulting in a higher accessibility of the DNAzyme to the target. As such, we used 0.001% of Tween20 surfactant for the remainder of this experiment.

Next, we used increasing units of M2 Motors to increase the number of DNAzymes on M2 Motors using the carbodiimide coupling between aminated DNAzymes and the carboxyl-rich backbone of M2 Motors (Figure S7) [57]. This was measured by monitoring the unreacted DNAzymes in solution following their incubation with the motors. Our results show that deposition at $4 \times 10^5$ units of M2 Motors at the lowest pH of 4.5 minimizes the amount of unbound DNAzymes. We hypothesize this finding to be due to the optimal carbodiimide covalent linking at a pH value of 4.5 [57].

To assess the performance of the Legionella Motolyzer during release and capture phases, we studied the kinetics of the assay under varying time-points (Figure S8). An increase in signal magnitude was observed from 15 to 30 min in the release and capture phases across all tested target concentrations. This finding aligns with previous investigations on the kinetics of DNA hybridization on electrodes, where longer incubation times increase the binding of target DNA strands [58, 59]. Interestingly, we noticed a decrease in signal magnitude for incubation times longer than 30 min, particularly for target concentrations lower than the stock concentration ($10^8$ CFU $mL^{-1}$). The decrease in signal magnitude may be explained by previous findings, where the presence of surfactant and fuel leads to protein denaturation [25] and degradation of electroactive redox molecules [60]. Based on these experiments, we selected 30 min for both the release and capture times for the rest of this study.

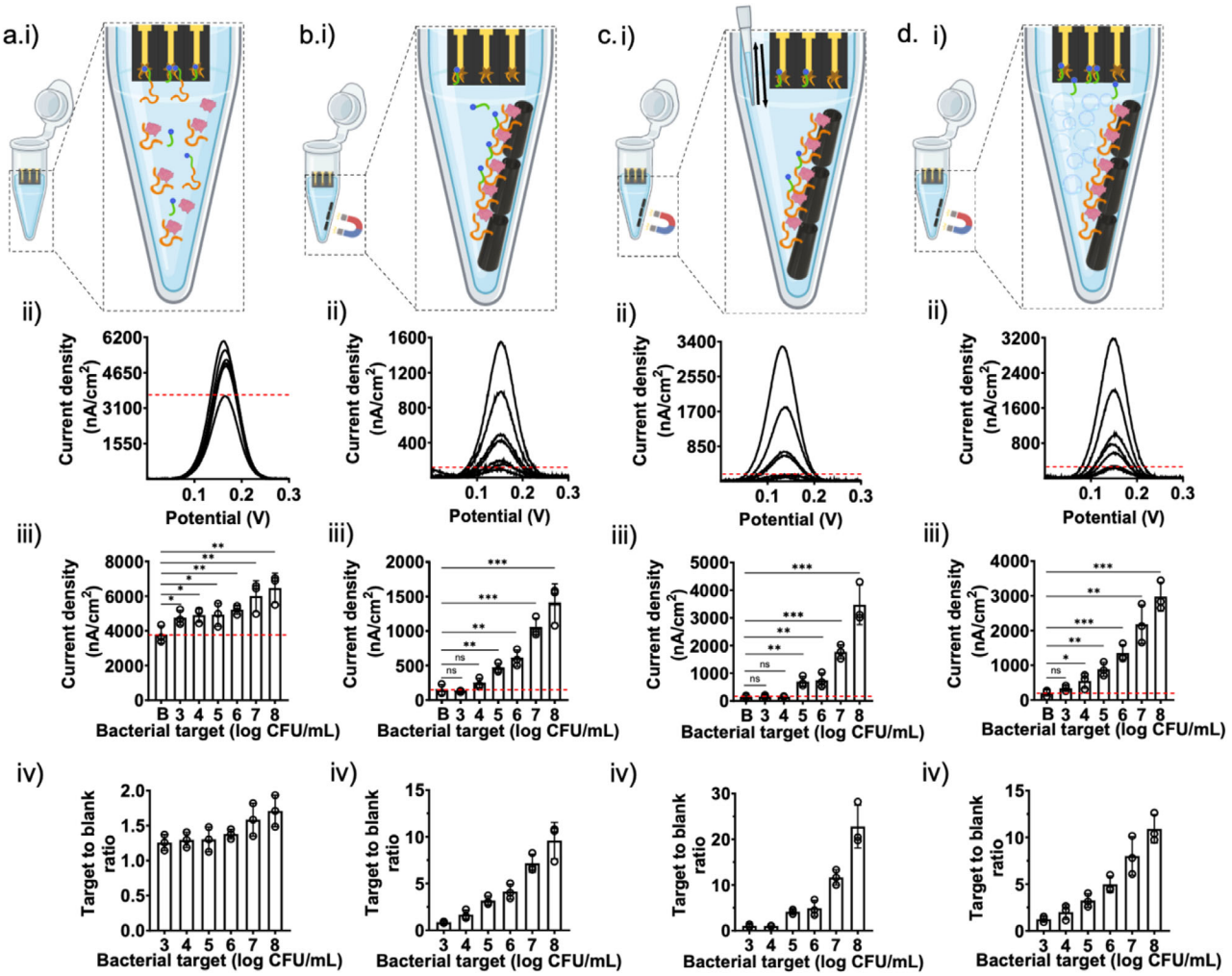


**FIGURE 3** | Comparison of the analytical performance of the Legionella Motolyzer against control assays. Evaluation of the (a) control assay lacking M2 Motors, (b) control assay including the M2 Motors but without fuel, (c) control assay involving manual agitation with a pipette, and (d) Legionella Motolyzer. (i) Schematic representation, (ii) square wave voltammograms, (iii) bar graphs representing the mean current measured at different concentrations, and (iv) target-to-blank ratio extracted from (iii) tested across different concentrations. All bar plots represent data from three separate chips with error bars representing standard deviation from the mean. Significance levels are indicated using asterisks (*$p < 0.05$, **$p < 0.01$, ***$p < 0.001$).

We hypothesized that active propulsion offered by M2 Motors increases assay sensitivity and enables the detection of lower target concentrations compared to conditions using static motors or manual agitation. To evaluate this hypothesis, we analyzed crude bacterial targets from $10^3$–$10^8$ CFU mL$^{-1}$ (10–$10^6$ CFU) using the Legionella Motolyzer, as well as three control setups (Figure 3a–c). One control set up eliminated M2 Motors entirely by utilizing DNAzymes that were free in solution (Figure 3ai). A second control was identical to the Legionella Motolyzer; however, it did not include $H_2O_2$ as the chemical fuel, resulting in M2 Motors that did not offer active propulsion (Figure 3bi). Lastly, a third control employed manual agitation, in which the sensing medium was manually agitated every 5 min using an external laboratory pipette (Figure 3ci). The Legionella Motolyzer assay (Figure 3di), as well as the control experiments, were performed using the optimized volume (120 µL) that yielded the highest signal-to-blank ratio (Figure S9). In the control case lacking M2 Motors, we did not observe the expected trend of increased signal with increased target concentration (Figure 3aii,iii). Even though we saw statistical differences between signals generated between blank and target signals from $10^3$ CFU mL$^{-1}$ to $10^8$ CFU mL$^{-1}$ concentrations, the assay demonstrated a low target to blank ratio (1.2–1.6) throughout the entire tested concentration range (Figure 3aiv). This lack of sensitivity is attributed to the partial hybridization of the DNAzyme to the DNA capture probes on the e-chips [61], making the assay insensitive to target concentration. In the case with inactive M2 Motors, an increasing trend in signal is observed with increasing target concentration (Figure 3bii,iii), with a current density of 1500 nA cm$^{-2}$ at the highest bacterial target concentration ($10^8$ CFU mL$^{-1}$), followed by a gradual decrease in signal magnitude with decreasing bacterial concentration. This assay provides a high target to blank ratio (0.5–9.5), which is sensitive to target concentration (Figure 3biv). The condition with manual agitation showed an overall increasing trend in current density as the target concentration increased (Figure 3cii,iii). However, for concentrations below $10^7$ CFU mL$^{-1}$, the current density dropped significantly, resulting in a non-log-linear relationship between signal and log of concentration. In contrast, the Motolyzer configuration with active motors exhibited a clear log-linear increase in signal with target concentration, yielding

higher current densities and target to blank ratios than the experiment with inactive motors without $H_2O_2$ (Figure 3cii,iii). Notably, active M2 motors produced approximately a two-fold increase in signal magnitude compared to inactive motors (Figure 3diii vs. 3biii) in the $10^5$–$10^8$ CFU $mL^{-1}$ range. This finding aligns with previously reported micromotor assays for C-reactive protein detection, where a 3-fold increase was observed under mixing conditions compared to static conditions [24, 25].

To compare how each assay configuration responded to increasing bacterial concentration, we performed an analysis of covariance (ANCOVA) using current density as the dependent variable, log(CFU) as a continuous covariate, and assay configuration (free DNAzyme, inactive motors, manual agitation, or the Motolyzer) as a categorical factor. The overall model was highly significant ($p < 0.0001$), indicating that bacterial concentration and assay configuration together explained most of the variability in signal. Both log(CFU) ($p < 0.0001$) and assay configuration ($p < 0.0001$) made significant independent contributions, demonstrating that (i) signal increases with bacterial concentration and (ii) the four configurations differ markedly in their overall signal levels after accounting for concentration. Importantly, the Motolyzer both achieved the best linearity (Figure S10; $R^2 = 0.9671$ vs. 0.8616 for inactive motors and 0.9536 for manual agitation) and the lowest limit-of-detection ($3.1 \times 10^4$ vs. $1.7 \times 10^6$ CFU $mL^{-1}$ for inactive motors and $1.9 \times 10^5$ for manual agitation).

To evaluate the reproducibility of Motolyzer, we calculated the relative standard deviation of the Motolyzer response across three independent chips. These values ranged from 12.5% at $2 \times 10^2$ CFU $mL^{-1}$ to 19.4% at $2 \times 10^3$ CFU $mL^{-1}$, 39.2% at $2 \times 10^4$ CFU $mL^{-1}$, 22.5% at $2 \times 10^5$ CFU $mL^{-1}$, 17.6% at $2 \times 10^6$ CFU $mL^{-1}$, 25.6% at $2 \times 10^7$ CFU $mL^{-1}$, and 13.9% at $2 \times 10^8$ CFU $mL^{-1}$ (Figure 3diii). These values demonstrate that the Motolyzer maintains reasonable reproducibility (<30%) across a wide range of bacterial concentrations, with high variation just below the assay's limit-of-detection.

Other electrochemical biosensors have been reported for the analysis of *L. pneumophilia* (Table S3). Even though some of the previously-reported systems demonstrate a lower limit-of-detection than Motolyzer, these approaches are constrained by complex sample preparation [62], long amplification steps [63], or dependence on fragile optical [63], electronic [64], fluidic [9] instrumentation. Instead, Motolyzer leverages actively propelled, magnetically separable micromotors to automate mixing and sensing, providing a balance between assay time, user-friendliness, and sensitivity.

According to the Center for Disease Control (CDC), the detection of *L. pneumophilia* for monitoring cooling tower water requires a limit-of-detection of ≤1000 CFU $mL^{-1}$ [65]. While our system does not currently meet this threshold, further optimization to the DNAzyme sequence and assay conditions could position our limit-of-detection within the required range in the future. Importantly, the use of active M2 Motors ($2 \times 10^4$ CFU $mL^{-1}$) resulted in a significant improvement over the limit-of-detection of inactive M2 motors ($1 \times 10^6$ CFU $mL^{-1}$) and manual agitation ($6.9 \times 10^5$ CFU $mL^{-1}$) (Figure S10), which presents an opportunity for optimizing the performance of other assays by leveraging the mixing capabilities of micromotors.

### 2.4 | Specificity of Motolyzer

To ensure the specificity of the Legionella Motolyzer toward *L. pneumophila*, we evaluated its performance against a panel of Gram-positive and Gram-negative bacteria, as well as environmental or clinical interferent targets: *Escherichia coli*, *Bacillus subtilis*, *Pseudomonas aeruginos*a, *Shigella sonnei*, *β*-Carotene algal metabolite, and human serum albumin (Figure 4a). As expected, when the Motolyzer was subjected to *L. pneumophila* targets, the largest current (Figure 4b) and target-to-blank ratio (15.4) was observed compared to when the device was exposed to other bacterial targets (0.8–1.4) (Figure 4c) [66]. Furthermore, the nonspecific signal falls below the upper (1946 nA $cm^{-2}$) and lower control thresholds (254 nA $cm^{-2}$), demonstrating remarkable specificity [67]. The high specificity observed in this assay is attributed to the stringent DNAzyme selection process [40]; as well as the two-phase DNAzyme cleavage and barcode capture processes that ensure that a signal is only generated in the presence of the right DNA barcode sequence. We also performed receiver-operating characteristic (ROC) analysis to quantitatively assess the assay's ability to discriminate L. pneumophila from all non-target species (Figure S11). The Motolyzer achieved an area under the curve (AUC) of 1.00 (95% CI: 1.00–1.00), indicating perfect classification performance across the tested panel. This ROC-based analysis confirms that the combination of sequence-specific DNAzyme cleavage and selective barcode capture yields exceptionally high specificity, even in the presence of structurally and functionally diverse interferents.

## 3 | Conclusion

In this study, we successfully developed an assay that leverages the unique properties of magnetic-layered micromotors (M2 Motors) to analyze crude biological samples for bacterial presence. This assay integrates M2 Motors, RNA-cleaving DNAzymes, and electrochemical readout, enabling rapid detection of *L. pneumophila* within 1 h. Our findings clearly demonstrate the advantages of utilizing M2 Motors compared to systems that either lack micromotors or the fuels necessary for their propulsion. The incorporation of micromotors enhances the target-to-blank ratio of the assay by an average 4.5 and 1.2 times compared to assays that do not utilize motors or fuels, respectively. Furthermore, the implementation of active micromotors improves the linearity of the assay compared to a case in which manual agitation was used for mixing. As a result of our assay design, we can identify *L. pneumophila* at a limit-of-detection of $2 \times 10^4$ CFU $mL^{-1}$ in just 1 h, without relying on the commonly used growth cultures, across a panel of Gram-positive and Gram-negative bacteria. The Motolyzer represents a powerful platform that can significantly enhance the performance of a wide range of electrochemical biosensors, meeting the requirements for limit-of-detection, specificity, speed, and simplicity in point-of-care testing. The current version of the Motolyzer is limited to analyzing small sample volumes, which could be particularly problematic for water analysis. We anticipate that the integration of the Motolyzer with microfluidics could help accommodate larger sample volumes, which would be critically important for the analysis of *L. pneumophila* in water. Furthermore, the future versions of the Motolyzer could include different barcode sequences released from various DNAzymes, enabling multiplexed analysis.

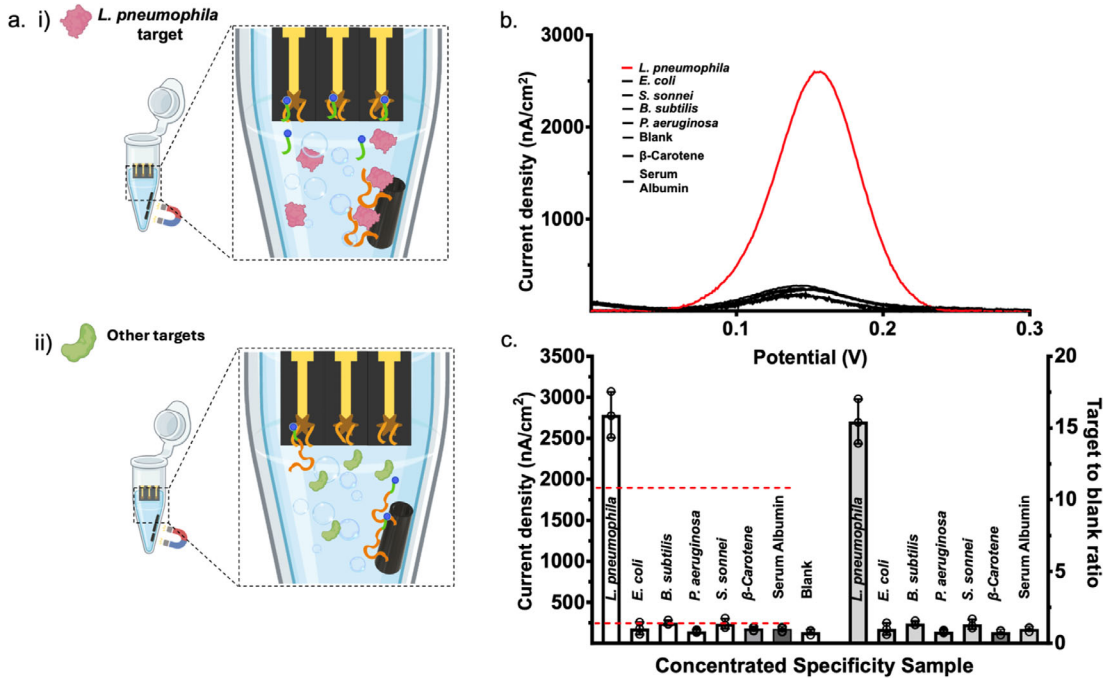


**FIGURE 4** | Evaluation of the specificity of the Legionella Motolyzer. (a) Schematic representation of the Motolyzer in the presence of specific (i) and non-specific (ii) targets. (b) Square wave voltammograms obtained from crude targets of *L. pneumophila*, *Escherichia coli*, *Bacillus subtilis*, *Pseudomonas aeruginosa*, and *Shigellasonnei*, which were harvested at $10^8$ CFU $mL^{-1}$, as well as *β*-Carotene (100 μM) and human serum albumin (10 mg/mL) added to micromotors functionalized with the *L. pneumophila* DNAzyme (total assay time: 1 h). (c) peak magnitudes (left *y* axis) and target to blank ratio (right *y* axis) for all tested specificity specimens used in this work. The dotted red lines illustrate the upper and lower control thresholds for distinguishing the target from blank, which are calculated as: upper threshold = average mean current of the specific target − 3 × standard deviation (specific target), lower threshold = average mean current of blank + 3 × standard deviation (blank). Each bar represents the mean data obtained using three different e-chips with error bars representing standard deviation from the mean.

## 4 | Experimental Section

### 4.1 | Materials

Polycarbonate membranes (5 μm pore size) were purchased from Whatman Cytiva (Cytiva life sciences, Massachusetts, United States). All DNA sequences and nuclease free water were purchased from Integrated DNA Technologies (IDT). Sodium chloride (NaCl, ≥99.0%), potassium chloride (KCl, ≥99.0%), phosphate buffer solution (1 M, pH 7.4), sodium sulfate anhydrous ($Na_2SO_4$, ≥99.0%) (magnesium chloride ($MgCl_2$, ≥99.0%), Tris(2-carboxyethyl)phosphine hydrochloride (TCEP), 100X Tris-EDTA (TE, pH 7.4), 6-mercapto-1-hexanol (MCH, 99%), potassium hexacyanoferrate(II) trihydrate ($[Fe(CN)_6]^{4-/3-}$, ≥99.95%), 10X tris borate-ETDA (TBE, pH ≈8.3), sodium cholate hydrate (BioXtra, ≥99%), urea (ACS reagent, 99.0–100.5%), gold (III) chloride solution ($HAuCl_4$, 30 wt% in HCl), chloroplatinic acid solution ($H_2PtCl_6$, 8 wt.%), nickel (II) chloride hexahydrate ($NiCl_2.6H_2O$, ≥99.9%), boric acid ($H_3BO_3$, ≥99.5%), nickel (II) sulfamate tetrahydrate ($Ni(SO_3NH_2)_2{\cdot}4H_2O$, 98%), graphene oxide (2 mg/mL dispersion in water), dichloromethane ($CH_2Cl_2$, ≥99.5%), bromophenol blue ($C_{19}H_{10}Br_4O_5S$, ACS reagent), xylene cyanol FF($C_{25}H_{27}N_2NaO_6S_2$, Bioreagent), sucrose ($C_{12}H_{22}O_{11}$, ≥99.5%), Tween20, N-hydroxysuccinimide ($C_4H_5NO_3$, 98%), and MES ($C_6H_{13}NO_4S$, ≥99%) were purchased from Sigma-Aldrich (Oakville, Canada). Sterile phosphate buffer solution (10X, pH 7.4), ammonium persulfate (APS), tetramethylethylenediamine (TEMED), SYBR Gold nucleic acid gel stain (10,000X in DMSO), acrylamide: bis-acrylamide 29:1(40% solution), 1-ethyl-3-(3-dimethylaminopropyl)carbodiimide hydrochloride (EDC), and dimethyl sulfoxide (DMSO) were purchased from Thermo Fisher Scientific (Mississauga, Canada). Hydrochloric acid (HCl, 37% w/w) were purchased from Labchem (Zelienople, United States). Ethyl alcohol anhydrous (100%) was purchased from Greenfield Global (Toronto, Canada). Hydrogen peroxide ($H_2O_2$, 30 wt.%) and HEPES ($C_8H_{18}N_2O_4S$, ≥99.5%), and Lysogeny (LB) broth (Miller, ≥99.5%) were purchased from BioShop Canada Inc. (Burlington, Canada). 2-propanol (99.5%) and sulfuric acid ($H_2SO_4$) were purchased from Caledon Laboratories (Georgetown, Canada). Methylene blue ester was purchased from Glen Research Institute ($C_{22}H_{23}N_4O_8SCl$) and dissolved in DMSO. All reagents were of analytical grade and were used without further purification. The water used in all experiments was purified using a Milli-Q A10 water purification system.

### 4.2 | E-chip Fabrication

The e-chips were fabricated on polystyrene sheets (Graphix shrink film, Graphix, Maple Heights, Ohio). First, the polystyrene sheet was sonicated in ethanol for 5 min followed by sonication in $ddH_2O$ water for 5 min and was dried with $N_2$ gas. A vinyl mask was then used to cover the polystyrene sheet (FDC 4304, FDC graphic films, South Bend, Indiana). The pattern from

e-chips was designed using Adobe Illustrator (version 29.2) and was cut into the design using a Robo Pro CE5000-40-CRP cutter (Graphtec, America Inc., Irvine, California). The outlined vinyl patterns were peeled from the polystyrene sheet, and 100 nm of gold (gold, 99.999% purity) was sputtered using a magnetron sputtering system at a vacuum pressure of $5 \times 10^{-3}$ Torr, a deposition rate of 0.6 $Å s^{-1}$, and current of 38 mA (CRC600 MagSput, New Windsor, United States). The vinyl mask was then removed to expose the desired design for assay use. The gold sputtered e-chips consisted of three star working electrodes for electrochemical measurements. The three working electrodes were rinsed with isopropyl alcohol using and $ddH_2O$ water, followed by electrodeposition of gold hierarchical structures. For this purpose, gold chloride ($HAuCl_4$) (10 mM) and HCl (0.5 mM) were nanostructured using an emstat3 potentiostat (Palmsens BV, Houten, Netherlands), with deposition performed at a potential of -0.6V for 500 s using Ag/AgCl as a reference electrode and a Pt wire as the counter electrode.

### 4.3 | Capture Probe Immobilization and E-chip Preparation for Assay

The hierarchical gold electrodes were rinsed with $ddH_2O$. Then, the electrodes were submerged in $H_2SO_4$ (0.1 M) and were cleaned using cyclic voltammetry (potential range: 0–1.5 V, scan rate: 0.1 V, cycles: 40). Then, the capture probe (3 μM) was treated with 100 times excess of TCEP for 2 h in the dark at room temperature, followed by deposition of 12 μL of reduced capture probe on triplicate star electrodes and the electrodes were incubated for 18 h at room temperature in the dark. After capture probe immobilization, 6 μL of MCH solution (100 mM) was deposited on the gold electrodes for 60 min in the dark at room temperature to block any exposed gold on the electrodes.

### 4.4 | Bacterial Target Preparation

*L. pneumophila* strains, serotype 1 (ATCC 33152) and serotype 2 (ATCC 33154) were obtained from the American Type Culture Collection (ATCC; Manassas, VA, United States). *L. pneumophila* was streaked on phosphate-buffered charcoal yeast extract agar plates for 3–4 days at 37°C in static conditions. A single colony was then inoculated into buffered yeast extract medium media with additional L-cysteine (3.3 mM), ferric pyrophosphate (0.33 mM). The liquid culture was incubated at 37°C, 250 rpm until an $OD_{600}$ of 1.0 was reached. The liquid culture was centrifuged 6,000 g for 5 min at 4°C. The supernatant was collected and passed through a 0.22 μm filter as crude extracellular matrix. Crude extracellular matrix aliquots were made and stored immediately at -80°C and were mixed in equal volume for experiments in this work. All other bacterial species used in this work were prepared using the same centrifugation, filtration, and storage conditions.

### 4.5 | Preparation of *L. pneumophilia* DNAzyme

The RNA-cleaving *L. pneumophila* DNAzymes were prepared using T4 DNA ligase-mediated ligation of the methylene blue-tagged substrate strand and the DNA Enzyme using a ligation template, as shown in Table S4. For tagging the substrate strand with methylene blue, 12 μL of methylene blue-NHS (in Dimethyl sulfoxide) was added and left at room temperature for 2.5 h, followed by overnight incubation in −20°C. The methylene blue-substrate strand was then purified using 10% denaturing polyacrylamide gel electrophoresis, isolated using ethanol precipitation, and stored in −20°C until further use.

For preparing the RNA-cleaving *L. pneumophila* DNAzyme, 1 nmole of DNAzyme was phosphorylated in a solution containing 1X polynucleotide kinase buffer, 4 mM adenosine triphosphate, and 20 U of the polynucleotide kinase buffer enzyme for 1 h at 37°C. The reaction was then heated at 90°C for 5 min to terminate the polynucleotide kinase reaction, and methylene blue-substrate strand (1.1 nmol) or the fluorescent substrate strand and ligation template (1 nmole) was added to the tube. The tube was then heated at 90°C for another 2 min followed by 15 min cooling at room temperature. The final concentrations of 1X DNA ligase buffer and 20 U of T4 DNA Ligase were added to the DNA sequences, and the ligation reactions were incubated overnight at 4°C. The ligated products were isolated using ethanol precipitation and purified using 10% denaturing polyacrylamide gel electrophoresis. The purified DNAzyme was then precipitated using ethanol precipitation and stored in −20°C until further use.

### 4.6 | Electrosynthesis of rGO/Ni/PtNP M2 Motors

Tubular rGO/Ni/PtNP M2 Motors were synthesized using template-assisted electrochemical deposition into the pores of a polycarbonate membrane as reported and optimized previously [50], with slight modifications. First, a 700 nm gold layer (gold, 99.999% purity) was deposited on one side of 0.5 μm conical pores of a polycarbonate membrane (Cytiva Life Sciences, Massachusetts, United States) using a magnetron sputtering system at a vacuum pressure of $5 \times 10^{-3}$ Torr, a deposition rate of 0.6 Å $s^{-1}$, and a current of 38 mA (CRC600 MagSput, New Windsor, United States). The sputtered membrane was assembled into a custom 3D-printed plating cell for subsequent deposition steps, with aluminum foil serving as an electrical contact to the sputtered gold working electrode. The outer rGO layer was deposited using CV (0−1.5 V, scan rate 50 mV $s^{-1}$, 6 cycles) via reduction of graphene oxide from a solution containing graphene oxide (0.1 mg $mL^{-1}$), $Na_2SO_4$ (0.5 M), and $H_2SO_4$ (0.1 M). The membrane was then rinsed with $ddH_2O$ water five times to remove excess graphene oxide sheets. Then, nickel was deposited galvanostatically from a solution containing nickel (II) sulfamate (1 M), nickel (II) chloride (80 mM), and boric acid (464 mM). First, 10 pulses at -20 mA were applied for 0.1s, followed by the growth of the nickel layer at −6 mA for 250 s. The membrane was then rinsed with $ddH_2O$ water five times to remove excess nickel-plating solution. Lastly, the platinum catalytic layer was deposited from a solution containing chloroplatinic acid (4 mM) and boric acid (0.5 M) amperometrically for 700 s at −0.4 V. The membrane was disassembled from the plating cell, and the deposited gold layer was removed by mechanical hand polishing with 4 μm alumina slurry. The membrane was dissolved in dichloromethane to release the micromotors, followed by 2 washing steps with isopropyl alcohol, ethanol, and $ddH_2O$

water. The micromotors were stored at 4°C in dd$H_2O$ water until further use.

### 4.7 | Micromotor Functionalization with *L. pneumophila* DNAzymes

The functionalization of micromotors was accomplished using the EDC/NHS carbodiimide coupling of amine-terminated *L. pneumophila* DNAzyme. For this purpose, approximately 400,000 of micromotors were washed with MES buffer (0.1 M, pH 6.5) twice, followed by 30 s of magnetic separation in between. Then, 40 µL of aminated methylene blue-tagged DNAzyme (1 µM), prepared in EDC/NHS (10 mM) (dissolved in 0.1 M MES buffer with 0.001% Tween 20, pH 4.5), was added to the micromotors and incubated at 4°C for 18 h.

### 4.8 | Micromotor Tracking and Trajectory

Motion videos (AVI) were analyzed in Fiji using the manual tracking plugin (Tracker). Pixel coordinates (X, Y) were exported as CSV for each frame. MATLAB was then used to convert pixels to micrometres, followed by computing frame times, velocities, and mean square displacement, and rendering color-coded trajectories with a fixed time scale bar. For multi-trajectory montage figures, the first point of each motor's track was set as the local origin and an (Δx, Δy), offset was applied in micrometres to layout multiple motors in one canvas.

### 4.9 | Mean Square Displacement

Mean square displacement was used to quantify the spatial spreading of micromotors over time. For a trajectory with coordinates $(x_i,y_i)$ at frame $i$, the squared displacement time for a lag $\tau = k \cdot \Delta t$ was defined as $(x_{i+k} - x_i)^2 + (y_{i+k} - y_i)^2$. The MSD at lag $\tau$ was calculated by averaging this squared displacement over all valid pairs of points in the trajectory:

$$MSD\ (\tau) = \frac{1}{N-k} \sum_{i=1}^{N-k} \left[ (x_{i+k} - x_i)^2 + (y_{i+k} - y_i)^2 \right]$$

where $N$ is the total number of frames, and $k$ is the lag in frame units. Mean square displacement values were averaged across five micromotors under identical experimental conditions to generate representative mean square displacement curves, while the standard deviation between motors was used to indicate variability.

### 4.10 | Limit-of-Detection Calculation

To calculate the limit-of-detection, the following parameters were obtained from the current density versus the log [crude extracellular matrix] plot, and were used to calculate the limit-of-detection as reported previously [59].

$$\text{Limit} - \text{of} - \text{blank} = \text{I}_{\text{target}-\text{blank}} + 1.65 \times \sigma_{\text{blank}}$$

$$\text{Limit} - \text{of} - \text{detection} = \text{LOB} + 65 \times \sigma_{\text{lowest detectable concentration}}$$

$$\text{Limit} - \text{of} - \text{detection}^{\text{bacterial CFU}} = \frac{\text{Limit} - \text{of} - \text{detection} - \text{y}}{\text{m}}$$

$$\text{Limit} - \text{of} - \text{detection in CFU mL}^{-1} = 10^{\text{limit}-\text{of}-\text{detection}}$$

where $\sigma_{\text{blank}}$ is the standard deviation of the blank signal, 1.645 is the score for a 95% confidence interval, m and y are the slope and y-intercept of the regression line.

### 4.11 | Statistical Analysis

All statistical analyses were performed using GraphPad Prism (10.3.0). The reported statistical parameters included the mean, standard deviation (SD), significant levels (n.s., not significant; *$p$ <0.05, ** $p$ <0.01, *** $p$ <0.001), and specific statistical tests used, which were described in detail in the figures and their respective captions. The significance of the statistical difference was calculated with 95% confidence interval ($\alpha = 0.05$). In all bar graphs representing current density, each data point represented the average of at least three different sensors ($n = 3$). Data were presented as mean ± SD. A p-value <0.05 was considered statistically significant, and the statistical significance between two-group comparisons was determined using a one-tailed *t*-test.

Calibration curves were analyzed using simple linear regression of current density versus $\log_{10}$ [CFU $mL^{-1}$]. Differences in slopes and intercepts between calibration lines were assessed using ANCOVA. Specificity was evaluated using receiver operating ROC analysis to obtain the AUC and its 95% confidence interval.

To calculate the relative standard deviation:

The relative standard deviation was used as a measure of reproducibility between replicate experiments. For a set of replicate values with mean $x$ and standard deviation $s$, the relative standard deviation was calculated as follows:

$$\text{relative standard deviation (RSD)} = \frac{\text{s}}{\text{x}} \times 100$$

to provide a normalized measure of variation independent of the absolute magnitude of the measurements, enabling comparison across different experimental conditions.

**Acknowledgements**

All electron microscopy measurements were performed at the Canadian Centre for Electron Microscopy (CCEM) at McMaster University. Leyla Soleymani is a Canada Research Chair in Miniaturized Biomedical Devices, as well as a Dorothy Killam Fellow and is supported by the Canada Research Chairs Program and the Killam Foundation. The work was supported by the Natural Sciences and Engineering Research Council of Canada (NSERC). All listed authors have significantly contributed directly and intellectually to the work and have given their approval for its publication.

## Conflicts of Interest

The authors declare no conflict of interest.

## Data Availability Statement

The data that support the findings of this study are available in the supplementary material of this article.

## References


1. L. Soleymani and F. Li, "Mechanistic Challenges and Advantages of Biosensor Miniaturization into the Nanoscale," *ACS Sensors* 2 (2017): 458–467.

2. T. M. Squires, R. J. Messinger, and S. R. Manalis, "Making it Stick: Convection, Reaction and Diffusion in Surface-Based Biosensors," *Nature Biotechnology* 26 (2008): 417–426.

3. A. Frutiger, A. Tanno, S. Hwu, R. F. Tiefenauer, J. Vörös, and N. Nakatsuka, "Nonspecific Binding—Fundamental Concepts and Consequences for Biosensing Applications," *Chemical Reviews* 121 (2021): 8095–8160.

4. P. R. Nair and M. A. Alam, "Performance Limits of Nanobiosensors," *Applied Physics Letters* 88 (2006): 233120.

5. O. Chailapakul, P. Ngamukot, A. Yoosamran, W. Siangproh, and N. Wangfuengkanagul, "Recent Electrochemical and Optical Sensors in Flow-Based Analysis," *Sensors* 6 (2006): 1383–1410.

6. N. S. Lynn, J.-I. Martínez-López, M. Bocková, et al., "Biosensing enhancement using passive mixing structures for microarray-based sensors," *Biosensors and Bioelectronics* 54 (2014): 506–514.

7. A. P. Iakovlev, A. S. Erofeev, and P. V. Gorelkin, "Novel Pumping Methods for Microfluidic Devices: A Comprehensive Review," *Biosensors* 12 (2022): 956.

8. X. Wang, C. Cheng, S. Wang, and S. Liu, "Electroosmotic Pumps and Their Applications in Microfluidic Systems," *Microfluidics and Nanofluidics* 6 (2009): 145–162.

9. E. Osman, S. Saxena, S. Qian, et al., "Electrochemical Detection of Legionella Pneumophila using DNAzymes and under Continuous Flow in Cooling Tower Water," *Biosensors and Bioelectronics* 278 (2025): 117283.

10. V. N. Goral, E. Tran, and P. K. Yuen, "A Pump-Free Membrane-Controlled Perfusion Microfluidic Platform," *Biomicrofluidics* 9 (2015): 054103.

11. V. Kamat, M. K. Grumbine, K. Bao, et al., "A Versatile Pumpless Multi-Channel Fluidics System for Maintenance and Real-Time Functional Assessment of Tissue and Cells," *Cell Reports Methods* 3 (2023): 100642.

12. A. A. Akhlaghi, H. Kaur, B. R. Adhikari, and L. Soleymani, "Editors' Choice—Challenges and Opportunities for Developing Electrochemical Biosensors with Commercialization Potential in the Point-of-Care Diagnostics Market," *ECS Sensors Plus* 3 (2024): 011601.

13. L. Soleymani, Z. Fang, E. H. Sargent, and S. O. Kelley, "Programming the Detection Limits of Biosensors Through Controlled Nanostructuring," *Nature Nanotechnology* 4 (2009): 844–848.

14. C. M. Miyazaki, E. Carthy, and D. J. Kinahan, "Biosensing on the Centrifugal Microfluidic Lab-on-a-Disc Platform," *Processes* 8 (2020): 1360.

15. B. T. Kelly, J.-C. Baret, V. Taly, and A. D. Griffiths, "Miniaturizing Chemistry and Biology in Microdroplets," *Chemical Communications* 18 (2007): 1773–1788.

16. D. Owen, M. Ballard, A. Alexeev, and P. J. Hesketh, "Rapid Microfluidic Mixing Via Rotating Magnetic Microbeads," *Sensors and Actuators A: Physical* 251 (2016): 84–91.

17. T. Mautner, "Application of the Synthetic Jet Concept to low Reynolds Number Biosensor Microfluidic Flows for Enhanced Mixing: A Numerical Study Using the Lattice Boltzmann Method," *Biosensors and Bioelectronics* 19 (2004): 1409–1419.

18. G. Bolat, E. De La Paz, N. F. Azeredo, et al., "Wearable Soft Electrochemical Microfluidic Device Integrated with Iontophoresis for Sweat Biosensing," *Analytical and Bioanalytical Chemistry* 414 (2022): 5411–5421.

19. J. Kim, I. Jeerapan, S. Imani, et al., "Noninvasive Alcohol Monitoring Using a Wearable Tattoo-Based Iontophoretic-Biosensing System," *ACS Sensors* 1 (2016): 1011–1019.

20. A. Renaudin, V. Chabot, E. Grondin, V. Aimez, and P. G. Charette, "Integrated Active Mixing And Biosensing Using Surface Acoustic Waves (SAW) and Surface Plasmon Resonance (SPR) on a Common Substrate," *Lab Chip* 10 (2010): 111–115.

21. Y. Huang, P. Kr Das, and V. R. Bhethanabotla, "Surface Acoustic Waves in Biosensing Applications," *Sensors and Actuators Reports* 3 (2021): 100041.

22. M. P. Nair, A. J. T. Teo, and K. H. H. Li, "Acoustic Biosensors and Microfluidic Devices in the Decennium: Principles and Applications," *Micromachines* 13 (2021): 24.

23. M. Guix, C. C. Mayorga-Martinez, and A. Merkoçi, "Nano/Micromotors in (Bio)Chemical Science Applications," *Chemical Reviews* 114 (2014): 6285–6322.

24. Á. Molinero-Fernández, M. Á. López, and A. Escarpa, "Electrochemical Microfluidic Micromotors-Based Immunoassay for C-Reactive Protein Determination in Preterm Neonatal Samples with Sepsis Suspicion," *Analytical Chemistry* 92 (2020): 5048–5054.

25. Á. Molinero-Fernández, L. Arruza, M. Á. López, and A. Escarpa, "On-the-Fly Rapid Immunoassay for Neonatal Sepsis Diagnosis: C-Reactive Protein Accurate Determination Using Magnetic Graphene-Based Micromotors," *Biosensors and Bioelectronics* 158 (2020): 112156.

26. R. Maria-Hormigos, B. Jurado-Sánchez, and A. Escarpa, "Surfactant-Free $\beta$-Galactosidase Micromotors for "On-The-Move" Lactose Hydrolysis," *Advanced Functional Materials* 28 (2018): 1704256.

27. Á. Gallo-Orive, M. Moreno-Guzmán, M. Sanchez-Paniagua, A. Montero-Calle, R. Barderas, and A. Escarpa, "Gold Nanoparticle-Decorated Catalytic Micromotor-Based Aptassay for Rapid Electrochemical Label-Free Amyloid-$\beta$42 Oligomer Determination in Clinical Samples from Alzheimer's Patients," *Analytical Chemistry* 96 (2024): 5509–5518.

28. C. C. Mayorga-Martinez and M. Pumera, "Self-Propelled Tags for Protein Detection," *Advanced Functional Materials* 30 (2020): 1906449.

29. D. Rojas, B. Jurado-Sánchez, and A. Escarpa, ""Shoot and Sense" Janus Micromotors-Based Strategy for the Simultaneous Degradation and Detection of Persistent Organic Pollutants in Food and Biological Samples," *Analytical Chemistry* 88 (2016): 4153–4160.

30. R. Dong, Q. Zhang, W. Gao, A. Pei, and B. Ren, "Highly Efficient Light-Driven $TiO_2$ –Au Janus Micromotors," *ACS Nano* 10 (2016): 839–844.

31. B. Jurado-Sánchez and A. Escarpa, "Janus Micromotors for Electrochemical Sensing and Biosensing Applications: A Review," *Electroanalysis* 29 (2017): 14–23.

32. M. Amouzadeh Tabrizi, M. Shamsipur, R. Saber, and S. Sarkar, "Isolation of HL-60 Cancer Cells From the Human Serum Sample Using $MnO_2$-PEI/Ni/Au/Aptamer as a Novel Nanomotor and Electrochemical Determination of Thereof by Aptamer/Gold Nanoparticles-poly(3,4-ethylene dioxythiophene) Modified GC Electrode," *Biosensors and Bioelectronics* 110 (2018): 141–146.

33. Y. Liu, Y. Zhang, F. Chen, M. Wang, J. Liu, and W. Hai, "Sensitive Detection of Infectious Disease Utilizing Carbon Sphere@$Fe_3O_4$ Micromotor Combined with Graphene Field-Effect Transistor," *Analytica Chimica Acta* 1315 (2024): 342804.

34. S. K. Panda, N. A. Kherani, S. Debata, and D. P. Singh, "Bubble-Propelled Micro/Nanomotors: A Robust Platform for the Detection of Environmental Pollutants and Biosensing," *Materials Advances* 4 (2023): 1460–1480.

35. E. Ma, K. Wang, and H. Wang, "An Immunoassay Based on Nanomotor-Assisted Electrochemical Response for the Detection Of Immunoglobulin," *Microchimica Acta* 189 (2022): 47.

36. J. M. Gordón Pidal, M. Moreno-Guzmán, A. Montero-Calle, et al., "Micromotor-Based Electrochemical Immunoassays for Reliable Determination of Amyloid-$\beta$ (1–42) in Alzheimer's Diagnosed Clinical Samples," *Biosensors and Bioelectronics* 249 (2024): 115988.

37. M. Liu, D. Chang, and Y. Li, "Discovery and Biosensing Applications of Diverse RNA-Cleaving DNAzymes," *Accounts of Chemical Research* 50 (2017): 2273–2283.

38. R. Pandey, D. Chang, M. Smieja, T. Hoare, Y. Li, and L. Soleymani, "Integrating Programmable DNAzymes with Electrical Readout for Rapid and Culture-Free Bacterial Detection Using a Handheld Platform," *Nature Chemistry* 13 (2021): 895–901.

39. V. Iliadi, J. Staykova, S. Iliadis, et al., "Legionella pneumophila: The Journey from the Environment to the Blood," *Journal of Clinical Medicine* 11 (2022): 6126.

40. S. Qian, E. M. McConnell, M. Rothenbroker, et al., "Detecting Legionella Pneumophila in Cooling Tower Water Samples with a DNAzyme/Bead-Based Fluorescence Assay," *Analysis & Sensing* 3 (2023): 202300020.

41. A. Ahmed, J. V. Rushworth, N. A. Hirst, and P. A. Millner, "Biosensors for Whole-Cell Bacterial Detection," *Clinical Microbiology Reviews* 27 (2014): 631–646.

42. I. O. Faniyi, O. Fasakin, B. Olofinjana, et al., "The Comparative Analyses of Reduced Graphene Oxide (RGO) Prepared Via Green, Mild and Chemical Approaches," *SN Applied Sciences* 1 (2019): 1181.

43. J. Chen, J. Wu, H. Ge, D. Zhao, C. Liu, and X. Hong, "Reduced Graphene Oxide Deposited Carbon Fiber Reinforced Polymer Composites for Electromagnetic Interference Shielding," *Composites Part A: Applied Science and Manufacturing* 82 (2016): 141–150.

44. L. Qiu, P. Liu, L. Zhao, et al., "Analysis of Plant Genomic Dnas and the Genetic Relationship Among Plants by Using Surface-Enhanced Raman Spectroscopy," *Vibrational Spectroscopy* 72 (2014): 134–141.

45. J. Ali, E. M. Bakhsh, N. Hussain, et al., "A new biosource for Synthesis of Activated Carbon and its Potential Use for Removal of Methylene Blue and Eriochrome Black T From Aqueous Solutions," *Industrial Crops and Products* 179 (2022): 114676.

46. D. Vilela, J. Parmar, Y. Zeng, Y. Zhao, and S. Sánchez, "Graphene-Based Microbots for Toxic Heavy Metal Removal and Recovery from Water," *Nano Letters* 16 (2016): 2860–2866.

47. E. Mishra, S. Majumder, S. Varma, and P. A. Dowben, "X-Ray Photoemission Studies of the Interaction of Metals and Metal Ions with DNA," *Zeitschrift für Physikalische Chemie* 236 (2022): 439–480.

48. R. Samba, "Is the Enhanced Adhesion of PEDOT Thin Films on Electrodes Due to Sulfur - Gold Interaction? - An XPS Study," *The Open Surface Science Journal* 5 (2013): 17–20.

49. J. Simmchen, V. Magdanz, S. Sanchez, et al., "Effect of Surfactants on the Performance of Tubular and Spherical Micromotors–A Comparative Study," *RSC Advances* 4 (2014): 20334.

50. A. Martín, B. Jurado-Sánchez, A. Escarpa, and J. Wang, "Template Electrosynthesis of High-Performance Graphene Microengines," *Small* 11 (2015): 3568–3574.

51. W. Gao, S. Sattayasamitsathit, J. Orozco, and J. Wang, "Highly Efficient Catalytic Microengines: Template Electrosynthesis of Polyaniline/Platinum Microtubes," *Journal of the American Chemical Society* 133 (2011): 11862–11864.

52. M. Moosavian, M. Moradzadeh, A. Ghadiri, and M. Saki, "Isolation and Identification of Legionella spp. in Environmental Water Sources Based on Macrophage Infectivity Potentiator (mip) Gene Sequencing in Southwest Iran," *AIMS Microbiology* 5 (2019): 223–231.

53. A. Mobed, M. Hasanzadeh, M. Agazadeh, A. Mokhtarzadeh, M. A. Rezaee, and J. Sadeghi, "Bioassays: The best alternative for conventional methods in detection of Legionella pneumophila," *International Journal of Biological Macromolecules* 121 (2019): 1295–1307.

54. E. S. Henle and S. Linn, "Formation, Prevention, and Repair of DNA Damage by Iron/Hydrogen Peroxide," *Journal of Biological Chemistry* 272 (1997): 19095–19098.

55. A. W. Peterson, "The Effect of Surface Probe Density on DNA Hybridization," *Nucleic Acids Research* 29 (2001): 5163–5168.

56. B. Liu, S. Salgado, V. Maheshwari, and J. Liu, "DNA Adsorbed on Graphene and Graphene Oxide: Fundamental Interactions, Desorption and Applications," *Current Opinion in Colloid & Interface Science* 26 (2016): 41–49.

57. B. Johnsson, S. Löfås, and G. Lindquist, "Immobilization of Proteins to a Carboxymethyldextran-Modified Gold Surface for Biospecific Interaction Analysis in Surface Plasmon Resonance Sensors," *Analytical Biochemistry* 198 (1991): 268–277.

58. J. I. Abdul Rashid, N. A. Yusof, J. Abdullah, and R. H. Shomiad @ Shueb, "Strategies in the Optimization of DNA Hybridization Conditions and its Role in Electrochemical Detection of Dengue Virus (DENV) Using Response Surface Methodology (RSM)," *RSC Advances* 13 (2023): 18748–18759.

59. E. Osman, S. Sakib, R. Maclachlan, et al., "A Comparison of DNA–DNA Hybridization Kinetics in Complex Media on Planar and Nanostructured Electrodes," *ACS Sensors* 9 (2024): 4599.

60. M. A. Ali, I. M. Maafa, and I. Y. Qudsieh, "Photodegradation of Methylene Blue Using a UV/$H_2O_2$ Irradiation System," *Water* 16 (2024): 453.

61. S. M. Imani, E. Osman, F. Bakhshandeh, et al., "Liquid NanoBiosensors Enable One-Pot Electrochemical Detection of Bacteria in Complex Matrices," *Advanced Science* 10 (2023): 2207223.

62. L. Jiang, R. Gu, X. Li, M. Song, X. Huang, and D. Mu, "Multiple Cross Displacement Amplification Coupled with Lateral Flow Biosensor (MCDA-LFB) for rapid detection of Legionella pneumophila," *BMC Microbiology* 22 (2022): 20.

63. M. A. Islam, W. M. Hassen, I. Ishika, A. F. Tayabali, and J. J. Dubowski, "Selective Detection of Legionella pneumophila Serogroup 1 and 5 with a Digital Photocorrosion Biosensor Using Antimicrobial Peptide-Antibody Sandwich Strategy," *Biosensors* 12 (2022): 105.

64. M. Gagliardi, M. Agostini, F. Lunardelli, et al., "Surface Acoustic Wave-Based Lab-on-a-Chip for the Fast Detection of Legionella Pneumophila in Water," *Sensors and Actuators B: Chemical* 379 (2023): 133299.

65. L. K. Pickering, C. J. Baker, G. L. Freed, et al., "Immunization Programs for Infants, Children, Adolescents, and Adults: Clinical Practice Guidelines by the Infectious Diseases Society of America," *Clinical Infectious Diseases* 49 (2009): 817–840.

66. P. Sen, Z. Zhang, S. Sakib, et al., "High-Precision Viral Detection Using Electrochemical Kinetic Profiling of Aptamer-Antigen Recognition in Clinical Samples and Machine Learning," *Angewandte Chemie International Edition* 63 (2024): 202400413.

67. M. Meshesha, A. Sardar, R. Supekar, et al., "Development and Analytical Evaluation of a Point-of-Care Electrochemical Biosensor for Rapid and Accurate SARS-CoV-2 Detection," *Sensors* 23 (2023): 8000.

**Supporting Information**

Additional supporting information can be found online in the Supporting Information section.

**Supporting File 1**: smtd70577-sup-0001-SuppMat.docx.

**Supporting File 2**: smtd70577-sup-0002-VideoS1.av.

**Supporting File 3**: smtd70577-sup-0003-VideoS2.avi.

**Supporting File 4**: smtd70577-sup-0004-VideoS3.avi.

**Supporting File 5**: smtd70577-sup-0005-VideoS4.avi.

**Supporting File 6**: smtd70577-sup-0006-VideoS5.avi.